RSC Advances

PAPER

View Article Online
View Journal | View Issue

Cite this: *RSC Adv.*, 2021, **11**, 147

Computational identification of potential chemoprophylactic agents according to dynamic behavior of peroxisome proliferator-activated receptor gamma†

Zhiwei Yang, *[abc] Yizhen Zhao,[a] Dongxiao Hao, [a] He Wang,[a] Shengqing Li,[d] Lintao Jia,[e] Xiaohui Yuan,[f] Lei Zhang,[a] Lingjie Meng [bg] and Shengli Zhang*[a]

Peroxisome proliferator-activated receptor gamma ($PPAR_\gamma$) is an attractive target for chemoprevention of lung carcinoma, however its highly dynamic nature has plagued drug development for decades, with difficulties in receptor modeling for structure-based design. In this work, an integrated receptor-based virtual screening (VS) strategy was applied to identify $PPAR_\gamma$ agonists as chemoprophylactic agents by using extensive docking and conformational sampling methods. Our results showed that the conformational plasticity of $PPAR_\gamma$, especially the H2 & S245 loop, H2′ & Ω loop and AF-2 surface, is markedly affected by binding of full/partial agonists. To fully take the dynamic behavior of $PPAR_\gamma$ into account, the VS approach effectively sorts out five commercial agents with reported antineoplastic properties. Among them, ZINC03775146 (gusperimus) and ZINC14087743 (miltefosine) might be novel $PPAR_\gamma$ agonists with the potential for chemoprophylaxis, that simultaneously take part in a flexible switch of the AF-2 surface and state change of the Ω loop. Furthermore, the dynamic structural coupling between the H2 & S245 and H2′ & Ω loops offers enticing hope for $PPAR_\gamma$-targeted therapeutics, by blocking kinase accessibility to $PPAR_\gamma$. These results might aid the development of chemopreventive drugs, and the integrated VS strategy could be conducive to drug design for highly flexible biomacromolecules.

Received 23rd October 2020
Accepted 12th December 2020

DOI: 10.1039/d0ra09059j

rsc.li/rsc-advances

1. Introduction

Peroxisome proliferator-activated receptor gamma ($PPAR_\gamma$), a ligand-activated transcription factor of the nuclear receptor (NR) superfamily, directly binds to and regulates the target genes involved in lipid and carbohydrate metabolism, cell proliferation, apoptosis, and angiogenesis. Recent preclinical study and epidemiological analysis postulate an important role for $PPAR_\gamma$ in carcinogenesis,[1,2] and $PPAR_\gamma$ agonists thiazolidinediones (TZDs, *e.g.* rosiglitazone, RSG) possess antiproliferative effects and stimulate apoptosis in lung carcinoma cell lines, especially non-small-cell lung cancer (NSCLC).[3,4] More interestingly, the cancer-preventing effects of several natural products are invariably associated with activation of $PPAR_\gamma$.[5–7] Existing evidence intensively indicates the latency of $PPAR_\gamma$ agonists in lung cancer chemoprevention, and stimulates a viable pursuit in chemoprophylactic agents.[8,9]

$PPAR_\gamma$ ligand-binding domain ($PPAR_\gamma$-LBD), which is necessary and sufficient for the transcriptional activation, is composed of 13 α-helices (H1–H12 and H2′), and includes a Y-shaped internal ligand-binding pocket (LBP) and an activation function-2 surface (AF-2, formed by H3-5 and H12, see Fig. 1).[10,11] The binding of endogenous and synthetic agonists to LBP causes conformational alterations in the AF-2 region to promote the displacement of a corepressor and the recruitment of a transcriptional coactivator, resulting in the activation and differentiation of gene expression.[10] Meanwhile, the β-sheet (surrounded by H2, H3 and H2′) and Ω loop can be mediators in the cyclin-dependent kinase 5 (Cdk5)-mediated $PPAR_\gamma$ phosphorylation at Ser245, which leads to the dysregulated expression of target genes.[11] Aiming at these conformational alterations, numerous efforts have been made to explore

[a]*MOE Key Laboratory for Nonequilibrium Synthesis and Modulation of Condensed Matter, School of Physics, Xi'an Jiaotong University, Xi'an 710049, China. E-mail: yzws-123@xjtu.edu.cn; zhangsl@xjtu.edu.cn; Fax: +86-29-82660915; Tel: +86-29-82660915*

[b]*MOE Key Laboratory for Nonequilibrium Synthesis and Modulation of Condensed Matter, School of Chemistry, Xi'an Jiaotong University, Xi'an 710049, China*

[c]*School of Life Science and Technology, Xi'an Jiaotong University, Xi'an 710049, China*

[d]*Department of Pulmonary and Critical Care Medicine, Huashan Hospital, Fudan University, Shanghai 200041, China*

[e]*State Key Laboratory of Cancer Biology, Department of Biochemistry and Molecular Biology, Air Force Medical University, Xi'an 710032, China*

[f]*Institute of Biomedicine, Jinan University, Guangzhou 510632, China*

[g]*Instrumental Analysis Center, Xi'an Jiao Tong University, Xi'an 710049, China*

† Electronic supplementary information (ESI) available. See DOI: 10.1039/d0ra09059j

selective full/partial agonists with distinct binding profiles.[11,12] Full agonists (*e.g.* RSG) in general favor direct contacts with AF-2,[13] while partial agonists (*e.g.* (2*S*)-2-(biphenyl-4-yloxy)-3-phenylpropanoic acid, LRG) occasionally stabilize the β-sheet/Ω loop (see Fig. 1).[13,14] Unfortunately, $PPAR_\gamma$-LBD is a highly dynamic entity with multiple low-energy conformations and ligand-dependent conformational dynamics, especially the AF-2, β-sheet and Ω loop regions (Fig. 1).[11,15,16] The highly structurally dynamic nature adds to not only the difficulties in advanced understanding of $PPAR_\gamma$ function, but also hinders the rational discovery of $PPAR_\gamma$ agonists.[15,16]

Nowadays, receptor-based virtual screening (RBVS) is routinely implemented in drug discovery to increase the efficiency of the development pipeline.[17] It not only allows successful predictions (*e.g.* antivirals for influenza and COVID-19) at the leading edge of a battle against a pandemic, but also provides a better understanding about the complexity of living systems.[18–22] Among the sequential stages of RBVS, the initial receptor structures have become a prerequisite for success, with a significant practical problem to determine the major physiological states or important transition states, especially for receptors with highly dynamic behavior.[23–25] To address this issue, a variety of algorithms and strategies have been developed for modeling receptor dynamics and minimizing disturbance of false positives, such as Markov state models (MSMs) and ensemble docking.[25–28]

In our previous works,[9,29] we applied an ensemble-based docking method to determine the binding profiles between ligands and $PPAR_\gamma$ with the ideal computational costs. The outcomes aroused our interest to integrate and extend existing flexible docking and conformational sampling methods to identify novel agents based on the dynamic behavior of $PPAR_\gamma$. In this work, an integrated RBVS strategy (Scheme 1) was proposed to identify $PPAR_\gamma$ agonists as cancer chemopreventive agents and their binding profiles, with the necessary flexibility to $PPAR_\gamma$-LBD, desirable chemical space of drug-like compound, and more cost-effective. The dynamic behavior of $PPAR_\gamma$-LBD (especially the AF-2, β-sheet and Ω loop regions) was firstly studied on a set of five representative structures by explicitly solvated molecular dynamics (MD) simulations, consisting of four crystal structures and a homology model (Fig. 1). Then, VS experiments were carried out against the ZINC library,[30] utilizing the multiple conformations exacted from the MD simulations. Ultimately, top ten compounds were selected for further MD simulations to clarify their binding profiles and interaction mechanisms. The data presented here showed that

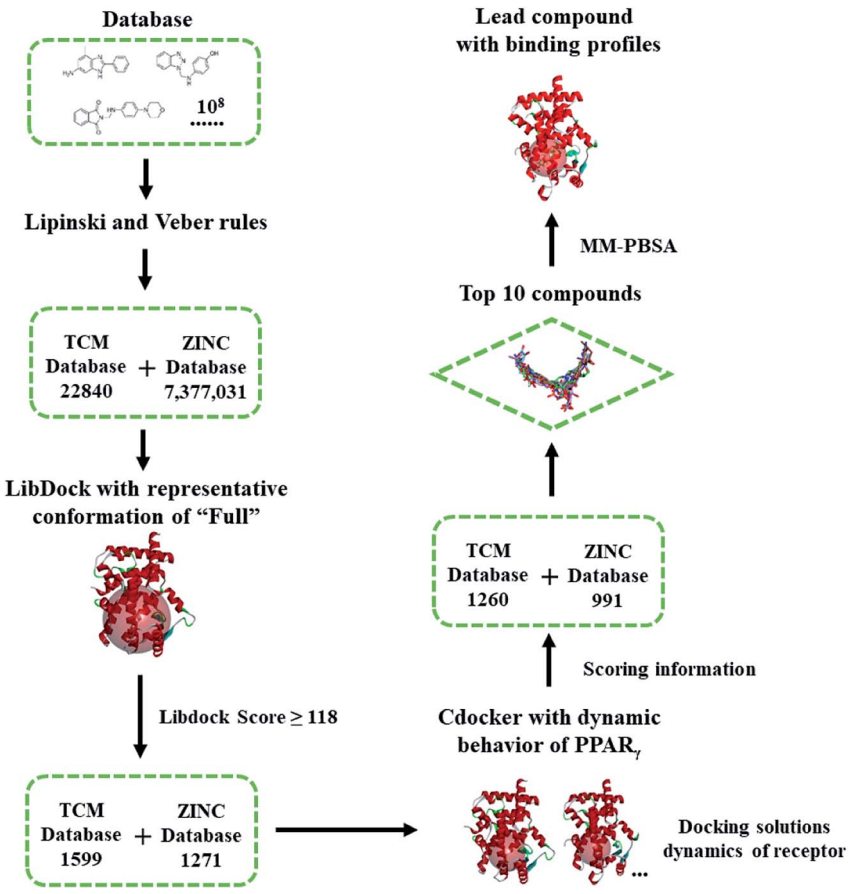

Scheme 1 Flowchart of virtual screening based on the dynamic behavior of $PPAR_\gamma$-LBD. The compounds were firstly filtered by rules formulated by Lipinski and Veber, then evaluated (LibDock) against a representative conformation of **Full**, with a 15.0 Å binding sites sphere. In terms of cDocker algorithm, representative conformations of **Full** and **Partial-1** were used with a 10.0 Å binding site sphere (conformation selection, see Fig. 2–4 and main text).

the remarkable flexibility of AF-2, β-sheet and Ω loop regions results in correspondingly different conformations of PPAR$_\gamma$, and five of selected compounds have been reported to the anti-tumor effects. Our results could be of value in the development of PPAR$_\gamma$ agonists with the chemopreventive effects, and the integrated VS strategy is expected to contribute to rational drug discovery of biomacromolecules with high dynamics.

2. Materials and methods

2.1. Representative structure setup

The coordinates of apo-active form (**Apo-active**, 1PRG[31]), active form with full agonist rosiglitazone (RSG) and coactivator peptide (**Full**, 1FM6 (ref. [32])), active form with partial agonist *S*-enantiomer of LRG (**Partial-1**, 3B3K[33]), and active form with partial agonist *R*-enantiomer of LRG (**Partial-2**, 3D6D[33]) were retrieved from RCSB Protein Data Bank. The apo-inhibition form with corepressor peptide (**Apo-inhibited**) was modelled using the MODELER module,[34,35] with the templates of PPAR$_\alpha$-LBD (1KKQ)[36] and 1PRG,[31] and then evaluated by Profile-3D module[35] and Procheck program.[37] Note that the differences between the five structures are shown in Fig. 1 and ESI Fig. 1.† All the hetero-atoms of non-protein parts were removed, and missing hydrogen atoms were added using Discovery Studio,[35] based on the expected charge distributions of amino acids at neutral pH.

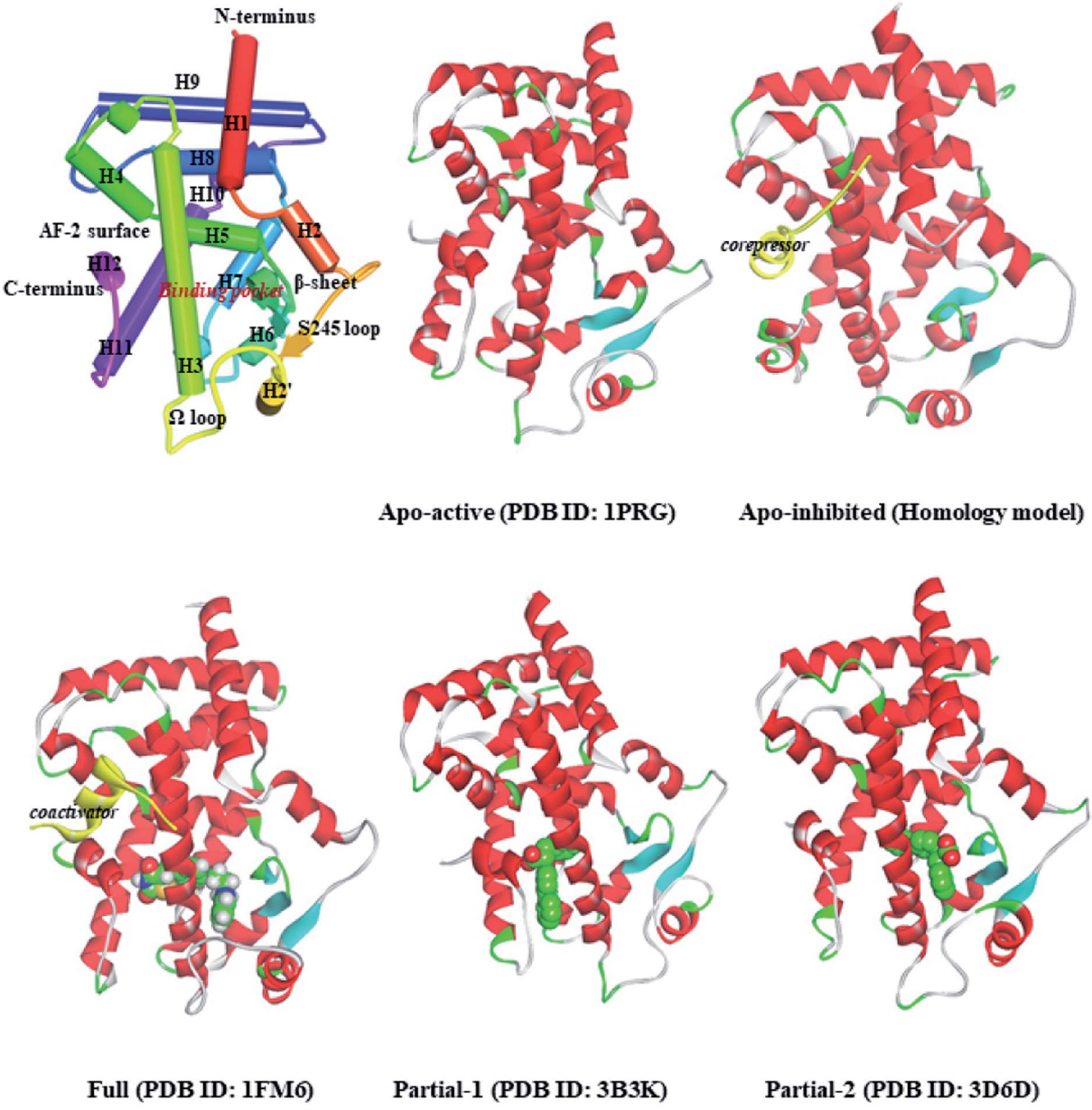

Fig. 1 Ribbon diagrams of PPAR$_\gamma$-LBD and five structures used in the simulations: **Apo-active**, apo-active form of PPAR$_\gamma$-LBD, **Apo-inhibited**, apo-inhibition form of PPAR$_\gamma$-LBD with corepressor peptide (in yellow), **Full**, active form of PPAR$_\gamma$-LBD with full agonist rosiglitazone (RSG) and coactivator peptide (in yellow), **Partial-1**, active form of PPAR$_\gamma$-LBD with partial agonist LRG^S (*S*-enantiomer of LRG), **Partial-2**, active form of PPAR$_\gamma$-LBD with partial agonist LRG^R (*R*-enantiomer of LRG).

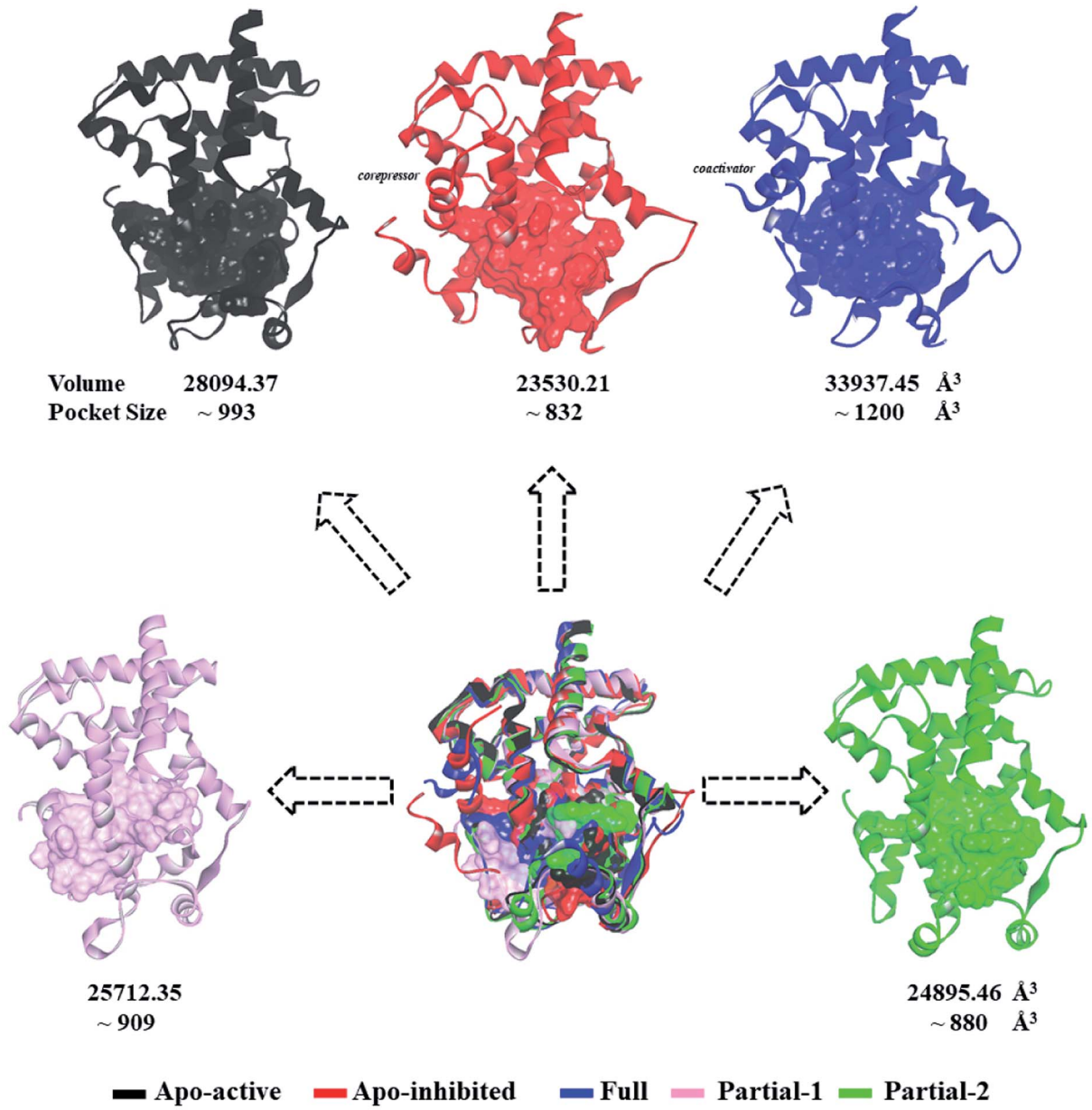

Fig. 2 Superimposition of various representative PPAR$_\gamma$-LBD conformations which were derived from simulation trajectories by using root mean-square difference (RMSD) clustering. The volumes and pocket sizes were separately determined by Discovery Studio client[35] and Fpocket program.[50]

The energy minimizations were performed with the Charmm27 force field,[38] until converged to 0.01 kcal mol^{-1} Å^{-1}. The explicit solvent MD simulations were conducted using GROMACS5.1.4 (ref. [39]) and the Charmm27 force field.[38] All investigated systems are summarized in Table 1, and the details of simulation setup are in agreement with our previous work.[9,20,29] In brief, each system was solvated in a cubic box of SPC/E (simple-point-charge) water molecules extending at least 9.0 Å from any solute atom. Na^+ counter-anions were placed to neutralize the system. To mimic physiological conditions, the NPT ensemble was applied at constant pressure (1 atm) and 300 K.[40] Particle-Mesh Ewald (PME) method[41] and LINCS algorithm[42] were applied to handle long-range electrostatics and constrain all covalent bonds. The cutoff radii for coulomb and van der Waals interactions were set to 8.0 Å. Free dynamics were performed using a 2.0 fs time step, and coordinates were collected every 10.0 ps. The representative conformation of each system was chosen using the g_cluster tool implemented in GROMACS.[43]

2.2. Virtual screening with representative structure

The 'Drugs-Now' and 'TCM Database @ Taiwan' subsets of ZINC database (downloaded on 28 August 2018)[30] were used in virtual screening, and firstly filtered by rules formulated by Lipinski (rule of five)[44] and Veber.[45] The selected compounds

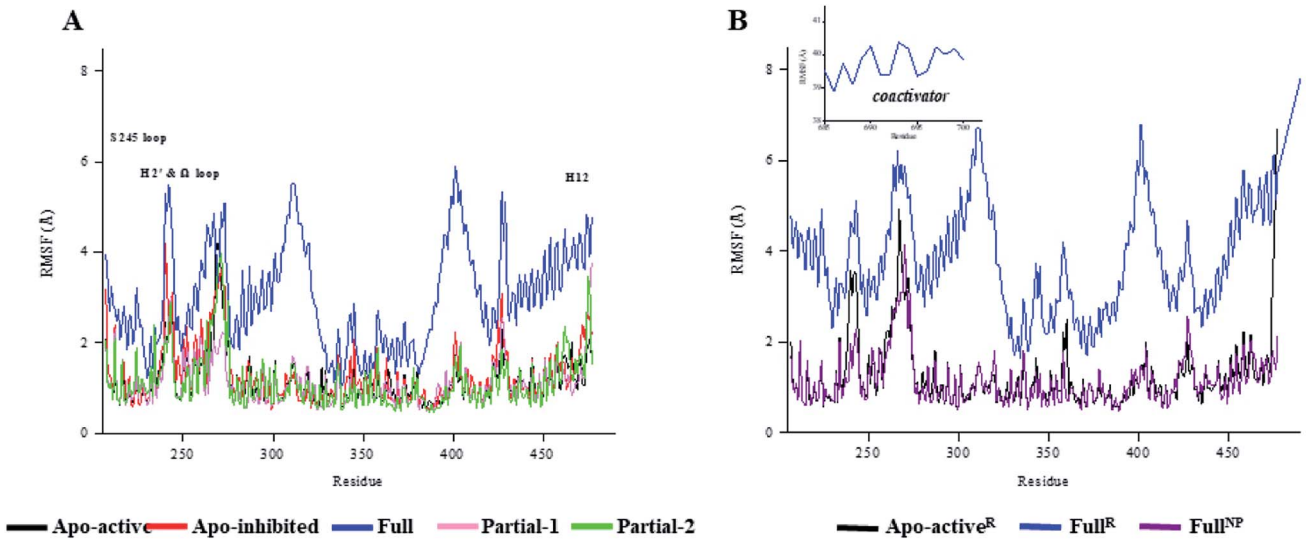

Fig. 3 The root-mean-square fluctuations (RMSF) per residue of various PPAR$_\gamma$-LBD structures over (A) 100 ns and (B) 600 ns MD trajectories. The values of **Full**^{R} were averaged based on three independent 600 ns MD trajectories. H2′ & Ω loop (residues 250–266 and residues 263–278), S245 loop (residues 237–253) and H12 (residues 465–477).

were then treated with 'Prepare Ligands' and 'Minimize Ligands' tools[35] to handle the geometries and partial atomic charges, especially correct ionization and low-energy conformers (converged to 0.001 kcal mol^{-1} Å^{-1}). Virtual screening was performed *via* two programs, LibDock[46] and cDocker.[47] The former is used for shape-based fast filtering, and the latter for semi-flexible fine screening. In our virtual screening protocol (see the flowchart of Scheme 1), the compounds were firstly evaluated (LibDock) against the MD-generated representative conformation of **Full**, with a 15.0 Å binding site sphere. The compounds with LibDock scores larger than those of full agonist RSG and partial agonist LRG^S (≥118), were selected for the second filter. In terms of cDocker algorithm, MD-generated representative conformations of **Full** and **Partial-1** were used, and the binding site was assigned with a sphere of 10.0 Å. The binding poses of best ten compounds were selected and further refined by 100.0 ns MD simulations. The details of screening parameters can be found in the ESI.†

2.3. Free energy calculation and geometric analysis

Binding free energies (ΔG_{bind}) were evaluated by the molecular mechanics generalized Born surface area method (g_mmpbsa),[48] which has been extensively used to expound the interactions between ligands and protein binding pockets.[9,29] Details of parameters are similar to those performed the previous works,[9,29] and in the ESI.† All values were calculated in averages over 200 snapshots evenly extracted from the 60–100 ns MD trajectories.

Apart from standard methods, secondary structures, volumes and binding pocket size were separately determined by the defined secondary structure of proteins (DSSP) method (do_dssp),[49] Discovery Studio client[35] and Fpocket program.[50] Principal component analysis (PCA) and dynamics cross-correlation matrices (DCCM) were calculated using Bio3D package[51] and GROMACS implemented tools.[39] Structural plotting and visualization were accomplished by Discovery Studio client.[35] Details of these analytical approaches can be found in the ESI.†

3. Results and discussion

3.1. Representative conformations and essential dynamics of PPAR$_\gamma$

First of all, dynamic behavior of PPAR$_\gamma$-LBD (especially the AF-2, β-sheet and Ω loop regions) was studied with the four crystal structures (**Apo-active**, **Full**, **Partial-1** and **Partial-2**) and one homology model structure (**Apo-inhibited**). Their structural differences have been shown in Fig. 1 and ESI Fig. 1,† and system setup of each MD simulation can refer to Table 1. The equilibration reliabilities were verified by monitoring the time evolution of structural parameters,[52] and each PPAR$_\gamma$-LBD structure (except **Full**) was well-behaved during the 100 ns MD simulations (ESI Fig. 2†), consistent with previous atomistic MD simulations of PPAR$_\gamma$-LBD with agonists.[9,29] As shown in Fig. 2, the representative conformations, extracted by RMSD clustering method, represent obvious structural differences. The representative conformation of **Full** has the maximal volume and pocket size with the values of ~33 937 and ~1200 Å^3, while those of **Partial-1** are moderate (~25 712 and ~909 Å^3) with the predictably different ligand-binding manner. While the volumes (pocket sizes) of **Apo-active**, **Apo-inhibited** and **Partial-2** are ~28 094 (~993), ~23 530 (~832) and ~24 895 (~880) Å^3. To further explore the structural adjustments, the root mean square fluctuations (RMSF) and principal component analysis (PCA) analyses were separately performed with the 60–100 ns MD trajectories using the GROMACS implemented tools[39] and Bio3D package.[51] According to the analysis results (Fig. 3 and 4), it was not difficult to observe that **Full**, **Partial-1** and **Partial-2**

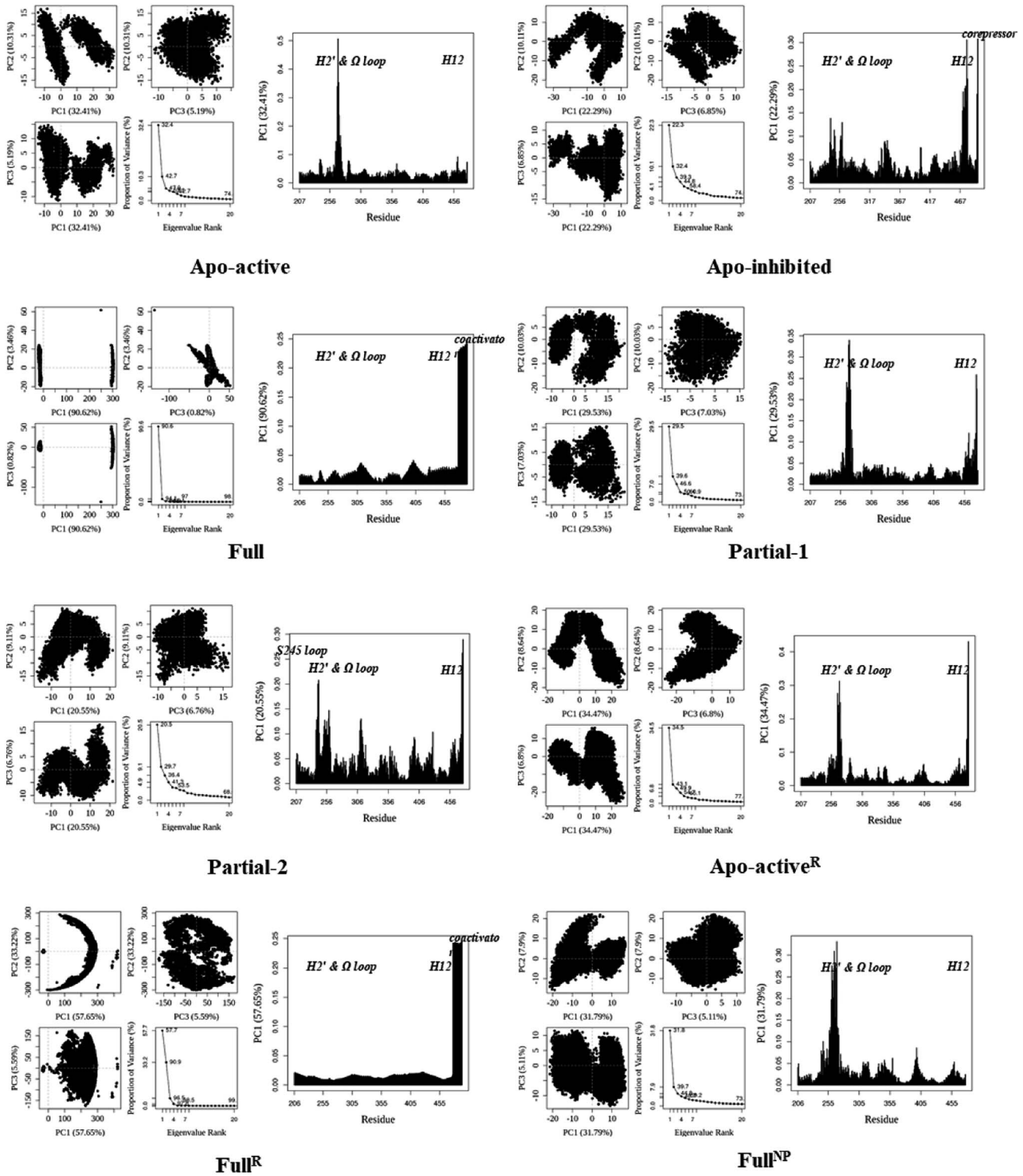

Fig. 4 Analysis of various PPAR$_\gamma$-LBD structures from MD simulations. Projection of snapshots onto the principal planes defined by the three most significant PCs (PC1, PC2 and PC3) *via* Bio3D package.[51] The magnitude of each eigenvalue is expressed as the percentage of the total variance (mean-square fluctuation) captured by the corresponding eigenvector. Eigenvalue rank was obtained from diagonalization of the atomic displacement correlation matrix of Cα atom coordinates. The analyses of **Apo-active^R**, **Full^R** and **Full^{NP}** were from 600 ns MD simulations, while others from 100 ns MD simulations (see ESI Fig. 2 and 3,† and main text).

exhibit dramatic fluctuations of S245 loop (residues 237–253), H2′ & Ω loop (residues 250–266 and residues 263–278) and H12 (residues 465–477). In addition, the overall correlated motions of **Full**, **Partial-1** and **Partial-2** are substantially dramatic, and their structures require a relatively long period to adjust and equilibrate, in which the AF-2, β-sheet and Ω loop regions

Table 1 Summary of each simulation and corresponding MD time-scale[a,b]

Simulation	System setup	Time (ns)
Apo-active	Apo-active PPAR$_\gamma$-LBD (PDB source: 1PRG chain A)	100
Apo-inhibited	Apo-inhibited PPAR$_\gamma$-LBD with corepressor (homology model)	100
Full	Active PPAR$_\gamma$-LBD with rosiglitazone and coactivator (PDB source: 1FM6)	100
Partial-1	Active PPAR$_\gamma$-LBD with partial agonist LRG^S (PDB source: 3B3K)	100
Partial-2	Active PPAR$_\gamma$-LBD with partial agonist LRG^R (PDB source: 3D6D)	100
Apo-active^R	Apo-active PPAR$_\gamma$-LBD (PDB source: 1PRG chain A)	600
Full^R (triplicate)	Active PPAR$_\gamma$-LBD with rosiglitazone and coactivator (PDB source: 1FM6, repeated for three times)	600
Full^{NP}	Active PPAR$_\gamma$-LBD with rosiglitazone (PDB source: 1FM6)	600

[a] Fig. 1 shows the corresponding structures. [b] All simulations include SPC/E water box, which extends at least 9.0 Å from any solute atom.

occupy the accessible conformations for the recruitment of co-regulator and agonist (Fig. 2–4), in accord with previous NMR and MD results.[10,15]

The dynamic features of apo-active PPAR$_\gamma$-LBD (**Apo-active^R**), active PPAR$_\gamma$-LBD with RSG and coactivator (**Full^R**), as well as active PPAR$_\gamma$-LBD with RSG (**Full^{NP}**) were further validated throughout the extra 600 ns MD simulations (Table 1 and ESI Fig. 3†). Note that the analyses of **Full^R** were performed over three replicate simulations to ensure the consistency of the individual simulations. The above-described motion patterns all reappeared, with more speculative locations of coactivator peptide within **Full^R**, viewed by RMSF and PCA results (Figure 3, 4, and ESI Fig. 4†). Structural fluctuates from our atomistic MD simulations reveal that the bound full/partial agonist (*e.g.* RSG/LRG) could consolidate the PPAR$_\gamma$-LBD conformations into active state, which favors coactivator binding (activation). While the H2′ & Ω loop, S245 loop and AF-2 surface (especially H12) are much perturbed during the agonist-interaction process (Fig. 2–4), in agreement with above descriptions.[10,15] Though the dynamic nature of PPAR$_\gamma$-LBD is restricted to favor coactivator binding with the present of RSG (**Full^{NP}** *vs.* **Apo-active^R**), the binding stability of coactivator peptide with PPAR$_\gamma$-LBD is less than previous affirmative expectations (**Full^R** *vs.* **Full^{NP}**).[13,53] It means that current full/partial agonists cannot fully facilitate the PPAR$_\gamma$ activation in modulating target gene expression, and may be attributed to the insufficient consideration of PPAR$_\gamma$-LBD dynamic behavior in rational design.[16,54] In fact, most of agonists were explored based on the steady-states of **Apo-active**, **Full** and **Partial-2**, with rarely considering the structural fluctuation of β-sheet and Ω loop regions (*e.g.* motion patterns of **Full** and **Partial-1**).[55–57] Thereby the representative MD-derived conformations of **Full** and **Partial-1** were adopted in the subsequent VS process to fully take the structural dynamics of AF-2, β-sheet and Ω loop regions, because of the dramatic motions (*e.g.* pocket size, structural fluctuation and ligand-binding manner, see Fig. 2–4).

3.2. Docking hits with representative conformations of PPAR$_\gamma$

Highly efficient and robust RBVS is a kind of art which aims at the achievement of balance between accurate optimization of ligand and receptor geometries, ligand–receptor complex representation and computational costs.[58] To take distinct ligand geometries, dynamic ensembles of PPAR$_\gamma$-LBD and effective efficiency into account in the docking procedures, an integrated VS platform (see Scheme 1) was applied to accurately predict the binding poses of candidates. The Lipinski (rule of five)[44] and Veber[45] rules quickly narrow the candidates ($\sim 10^8$) down to 22 840 (TCM) and 7 377 031 (ZINC) compounds, with reasonable drug-like physicochemical properties. Site feature docking (LibDock[46]) ulteriorly picks out 1599 (TCM) and 1271 (ZINC) compounds to form favorable binding interactions, using the protein site feature of MD-generated conformation of **Full** which has the maximal internal pocket size. Note that this motion not only ensures the chemical space of filtered compounds, but also successfully sorts out positive controls RSG and LRG^S, with the LibDock score of ~118. In terms of cDocker algorithm,[47] MD-generated conformations of **Full** and **Partial-1** present the representative dynamic features, and the predicted binding poses of RSG and LRG^S with **Full** and **Partial-1** are in a manner consistent with the crystallographic poses (1FM6 and 3B3K), with the cDocker interaction energies (E_{int}) being −61.29 and −66.62 kcal mol^{-1}, respectively (ESI Table 1†). As is evident, 1260 (TCM) and 991 (ZINC) compounds selectively bind with **Full** and **Partial-1** (Scheme 1), and the binding patterns of evaluated top ten compounds seem separately to be comparable to those of RSG and LRG^S (ESI Fig. 5†). Among the top ten compounds, compound ZINC15120682 and ZINC85568445 are the natural products (TCM), and other eight compounds are commercial agents, with one of them (ZINC12381030) being the proved PPAR agonist (ESI Scheme 1†).[30] More important, several experimental studies have shown the five commercial agents ZINC03775146 (gusperimus),[59] ZINC03831462 (sofalcone),[60] ZINC14087743 (miltefosine),[61] ZINC17719775 (ascorbyl palmitate)[62] and ZINC58581064 (dolutegravir)[63] to have the miscellaneous antineoplastic activities, especially hindering the signal transduction of cellular proliferation. The binding properties will be further discussed in the following section.

3.3. Binding features of compounds predicted by MM–PBSA

As shown in ESI Fig. 6 and 7,† each docked complex reached the fundamental convergence after ~40 ns, indicated by the time evolutions of backbone-atom and ligand positional RMSDs, and

interaction energy profiles (short-range energy components).[64,65] It reveals that a 100 ns simulation is sufficient for the structural relax, and relatively stable MD trajectories (60–100 ns) are subsequently selected for further analyses of energy and geometry.[9,29] In accord with our simulations, ZINC03775146 (gusperimus), ZINC03831462 (sofalcone), ZINC14087743 (miltefosine) and ZINC17719775 (ascorbyl palmitate) are preferred agonists, with the average binding free energies (average between values of **Full** and **Partial-1**, ΔG_{bind}) being −109.04, −8.12, −22.94 and −34.91 kcal mol^{-1}, respectively (Table 2). Note that the ΔG_{bind} values of RSG and LRG^{S} with PPAR$_\gamma$-LBD are −40.04 and −43.23 kcal mol^{-1}, respectively. van der Waals components (ΔE_{vdw} + ΔG_{sur}) primarily drive the binding processes of the four compounds, with the contributions over −48 kcal mol^{-1}, which is consistent with previous MD simulations of PPAR$_\gamma$-LBD with agonists (ESI Tables 2 and 3†).[9,29] In contrast to current agonist (*e.g.* RSG/LRG), the four compounds seem to induce more favorable coactivator binding, with the possibly preferable PPAR$_\gamma$ activation (Fig. 5 and ESI Fig. 5–7†).

ZINC03775146 (gusperimus) is a conventional immunosuppressor drug with the antitumor activities.[59] It can enter and fill the ligand-binding pocket (LBP) of PPAR$_\gamma$-LBD (**Full**), with the binding pose resembling that of full agonist RSG (Fig. 5A). Guanidino group of ZINC03775146 has electrostatic (H-bonding) interactions with residue Glu259 of H2′, residues Leu270 and Ser274 of Ω loop. *N*-(Hydroxymethyl)acetamide group of ZINC03775146 occupies the portion of the large two-lobe entry of the pocket,[13,66] where residue Arg288 of H3, residues Leu340 and Ser342 of β-sheet region are in electrostatic contacts. ZINC03775146 also has H-bonding interactions with residue Ser289 of H3 and residue Tyr473 of H12 (Fig. 5A). In addition, the alkyl portion of ZINC03775146 has hydrophobic stacking with residues Cys285 (H3) and Tyr327 (H4/5). ZINC03831462 (sofalcone)[60] normally treats gastric ulcer and chronic gastritis, and upregulates the nuclear factor (erythroid-derived 2)-like 2/heme oxygenase-1 pathway. Its binding with **Partial-1** is close to the case of partial agonist LRG^{S} (Fig. 5B). ZINC03831462 demonstrates hydrophobic interactions with residues Cys285 and Arg288 of H3, residues Leu330 and Leu333 of H4/H5, residues Met364 and Lys367 of H7, residues His449, Leu453, Ile456 and Lys457 of H11, as well as residue Leu469 of H12. The result agrees with a previous proposal that PPAR$_\gamma$ partial agonists interact with residues inside the region between H3 and β-sheet (Fig. 1), thereby promoting the stabilization of β-sheet surface.[67,68] ZINC14087743 (miltefosine)[61] is an oral drug used for the treatment of visceral leishmaniasis, can inhibit phosphatidylinositol-3-kinases (PI3K)/protein-serine–threonine kinase (Akt) activity in the cancer cell lines A431 and HeLa. It occupies the canonical binding pocket of PPAR$_\gamma$-LBD, with the binding pose resembling those of RSG and ZINC03775146 (Fig. 5C and ESI Fig. 5†). Residues Arg280, Phe282 and Gly284 of H3, residue Phe363 of H7, residues His449 and Leu453 of H11, residue Glu259 of H2′, residues Leu270 and Ser274 of Ω loop, as well as residue Ser342 of β-sheet region are in hydrophobic contacts within the ZINC14087743–**Full** complex. The binding of ZINC17719775 (ascorbyl palmitate, an antioxidant)[62] with **Partial-1** is close to the cases of LRG^{S} and ZINC03831462 (Fig. 5D). However, only residues Glu460, Met463 and Leu465 of AF-2 (portion of H11 and H12) are in hydrophobic interactions with ZINC17719775.

3.4. Insights about structural movements of PPAR$_\gamma$ and chemoprophylactic agents

In general, full agonists (*e.g.* RSG) adopt a common horseshoe conformation centered about H3 to stabilize the AF2 surface (Fig. 1), and have the extensive hydrogen bond network with residues Ser289, His323, His449 and Tyr473.[13] Instead, partial agonists (*e.g.* LRG) bind in the part of LBP with a hydrophobic manner (*e.g.* residue Cys285) and stabilize the β-sheet (*e.g.* residue Ser342)/Ω loop.[13,14] Our MD results indicated that the top four compounds are located near the canonical LBP of PPAR$_\gamma$-LBD, associated with the stabilization of AF-2 (*e.g.* residue Leu453 of H11, and residues Leu465, Leu469 and Tyr473 of H12, Fig. 5 and ESI Fig. 5†). This motion is similar as the cases of current full/partial agonists, while shows relatively few H-bonding interactions with H12 (Fig. 5).[10,15] The four

Table 2 Docking results of top ten compounds (binding free energies, ΔG_{bind})[a]

#	ZINC no.	Vendors	Catalog number	**Full**	**Partial-1**	Average
1	**ZINC03775146**	**AK Scientific**	**K529**	**−124.17**	**−93.90**	**−109.04**
2	**ZINC03831462**	**3B Scientific Corporation**	**3B2-0795**	**−4.16**	**−12.09**	**−8.12**
3	ZINC15120682	—	—	−0.92	15.31	7.20
4	ZINC12381030	Vitas-M	STK170412	14.60	20.74	17.67
5	**ZINC14087743**	**BioSynth**	**M-7200**	**−24.58**	**−21.29**	**−22.94**
6	ZINC03874917	3B Scientific Corporation	3B3-013268	18.02	29.13	23.58
7	**ZINC17719775**	**Acros Organics**	**44 948**	**−29.52**	**−40.29**	**−34.91**
8	ZINC03874915	3B Scientific Corporation	3B3-013268	35.25	36.13	35.69
9	ZINC58581064	AK Scientific	X7595	6.69	9.12	7.91
10	ZINC85569445	—	—	24.85	29.74	27.30
	RSG[b]	Vitas-M	STL350047	−40.04	—	−40.04
	LRG^{Sc}	—	—	—	−43.23	−43.23

[a] Energy units in kcal mol^{-1}, obtained from the equilibrium structures. [b] Rosiglitazone, control for full agonist. [c] *S*-(2*S*)-2-(Biphenyl-4-yloxy)-3-phenylpropanoic acid, control for partial agonist.

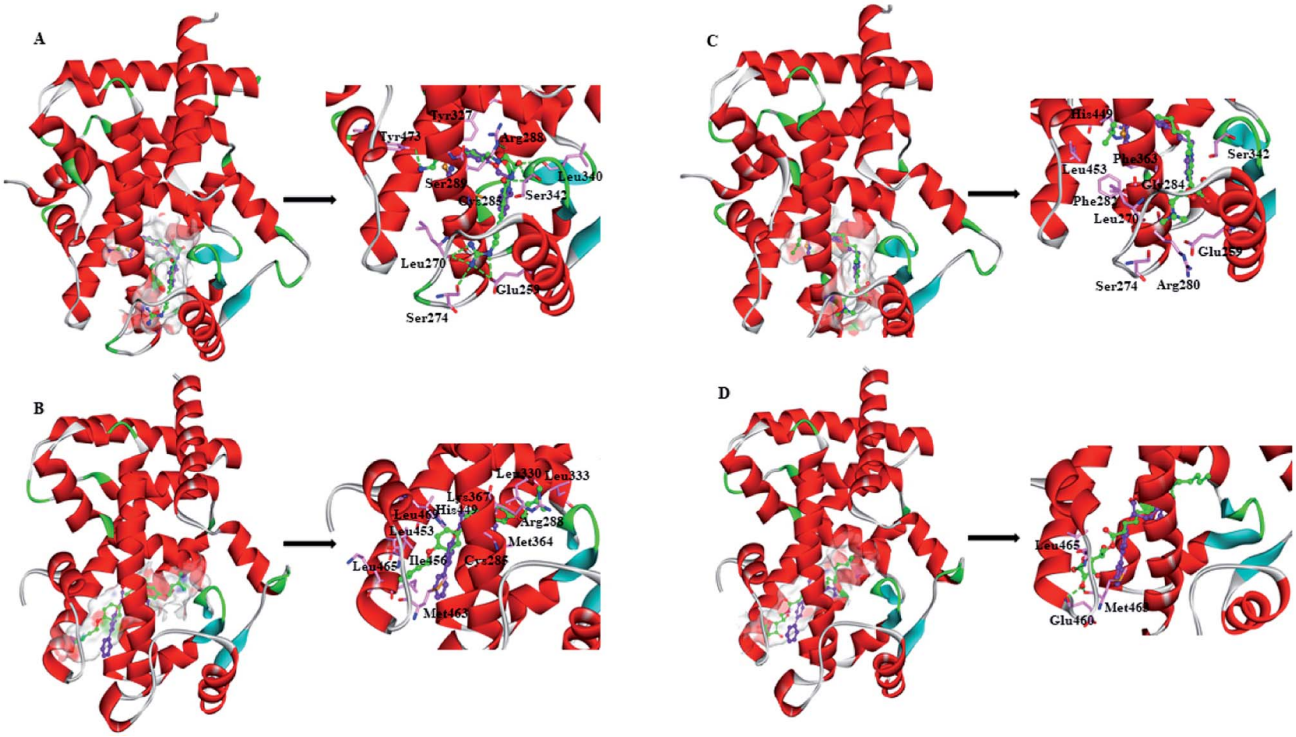

Fig. 5 Views of the preferred binding modes of selected compounds with the active-site residues of PPAR$_\gamma$-LBD: (A) ZINC03775146–**Full**, (B) ZINC03831462–**Partial-1**, (C) ZINC14087743–**Full** and (D) ZINC17719775–**Partial-1**. Key residues are represented by stick models, with C atoms in pink. Compounds are represented by ball and stick models. The O, N, C, S atoms are colored in red, blue, green and dark yellow, respectively. The important H-bonds (or electrostatic interactions) are labeled in the dashed black lines. For comparison, cocrystallized orientation of rosiglitazone (RSG) and *S*-(2*S*)-2-(biphenyl-4-yloxy)-3-phenylpropanoic acid (LRG^S) within **Full** and **Partial-1** are shown in ball and stick models, with C atoms in purple.

compounds take a middle-of-the-road approach, and supplement the hydrophobic (H-bonding) interactions with few important residues of H3 (*e.g.* residue Cys285 and Arg288), β-sheet (residue Ser342) and Ω loop (*e.g.* residues Leu270 and Ser274) regions, especially ZINC03775146 (gusperimus) and ZINC14087743 (miltefosine). For all this, the residue fluctuations of H12 remain relatively stable, however those in the ZINC03775146/ZINC14087743 bound complexes have much larger changes (Fig. 5, ESI Fig. 5 and 6†). It indicates that H12 of the four bound complexes occupies more stability (less subensembles), seemed to correlate positively with agonist activity. For instance, RSG holds the H12 in narrow energy well with rare structural exchange, and has the substantial IC$_{50}$ value.[15,33]

To further explore the influence of the four compounds on the structural movements of PPAR$_\gamma$-LBD, the large amplitude conformational changes and secondary structure alterations were monitored during the 100.0 ns MD simulations (Fig. 6 and 7). H2 & S245 loop and H2′ & Ω loop in ZINC03775146–**Full** and ZINC14087743–**Full** exhibit a much larger fluctuation than those in the other two bound complexes, especially residues Thr238 and Gly239 of H2, residues Ser245 and Pro246 of S245 loop, and residues Leu270 and Ser274 of Ω loop (Fig. 6 and 7). These results intensely indicate that H2 and H2′ of **Full** with the present of ZINC03775146 (gusperimus)/ZINC14087743 (miltefosine) turn the conformational alteration process over to the configuration adjustment of Ω loop (adjacent to H2′), to achieve an optimal fit of compound with the PPAR$_\gamma$-LBD (Fig. 5 and ESI Fig. 5†). This observation agrees with the previous points that some partial agonists likely induce a closed state of the Ω loop, to inhibit the PPAR$_\gamma$ phosphorylation induced by Cdk5.[57,68] The differences in dynamic cross-correlation maps (DCCM) between the four docked complexes further support the altered motions of the S245 and Ω loops upon binding of the corresponding compound (ESI Fig. 8†). So in conclusion, the binding of selective compound (at least ZINC03775146, gusperimus) induces the conformational adjustments of the PPAR$_\gamma$-LBD (*e.g.* H12 and Ω loop regions), associated with the correlated motions (shared community) between H2 & S245 loop and H2′ & Ω loop regions, that analogously viewed by the conformational dynamics of allosteric proteins.[54] Consequently, the four compounds could be looked as a new class of agonist, in view of AF-2 surface's flexible switch (full agonist-like binding model) and Ω loop's state change (partial agonist-like binding model) simultaneously (Fig. 1 and 5). More importantly, the middle-of-the-road approach of ZINC03775146 (gusperimus) and ZINC14087743 (miltefosine) with PPAR$_\gamma$ gives conceivable clues to explain the relevance of them in inhibiting and blocking the signal transduction of cellular proliferation, as well as the inhibitions of cancer cells.[59,61] Thereby ZINC03775146 (gusperimus) and ZINC14087743 (miltefosine) may be preferred PPAR$_\gamma$

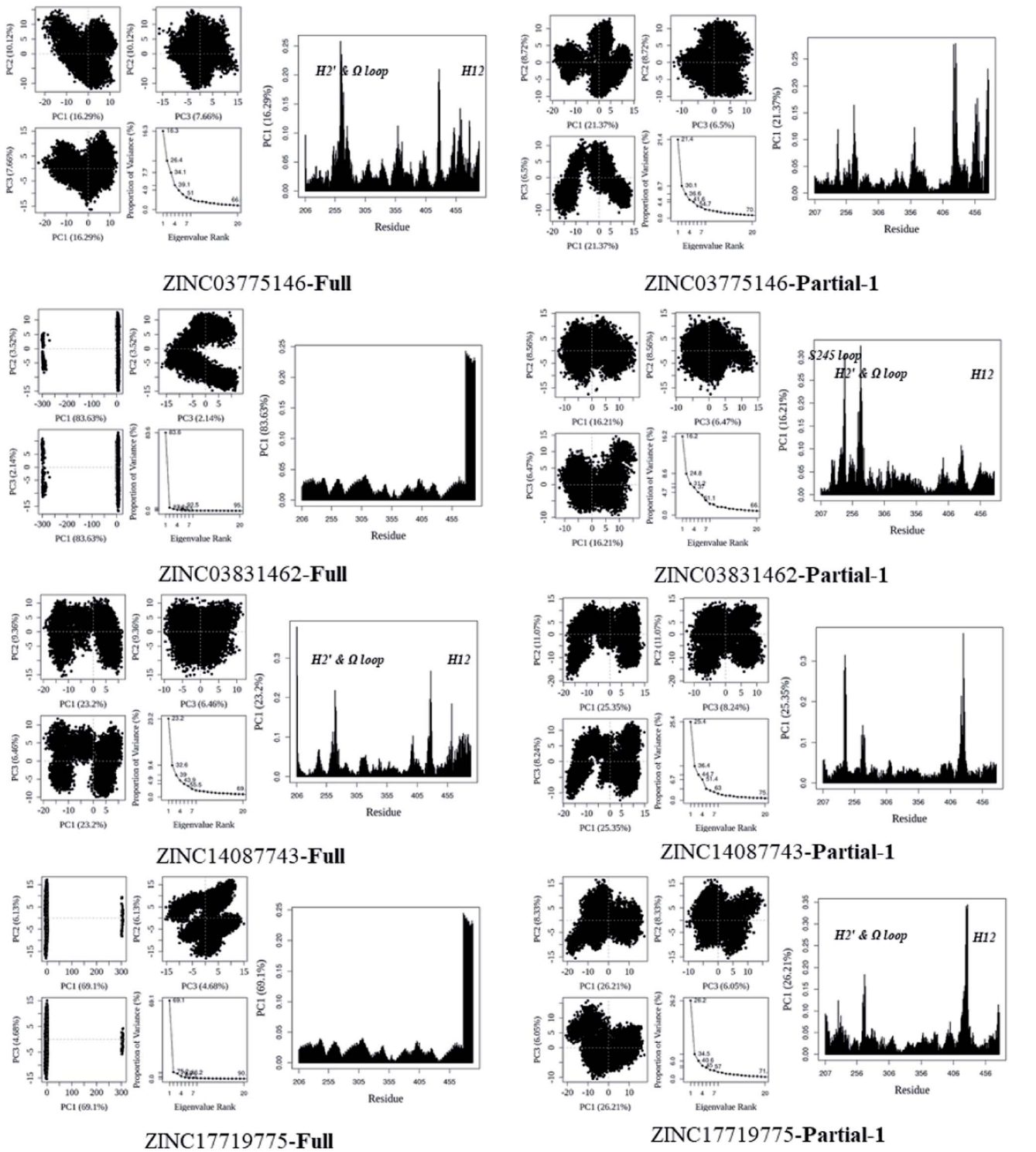

Fig. 6 Analysis of various docked complexes from MD simulations. Projection of snapshots onto the principal planes defined by the three most significant PCs (PC1, PC2 and PC3) *via* Bio3D package.[51] The magnitude of each eigenvalue is expressed as the percentage of the total variance (mean-square fluctuation) captured by the corresponding eigenvector. Eigenvalue rank was obtained from diagonalization of the atomic displacement correlation matrix of Cα atom coordinates. The analyses were from 100 ns MD simulations (see ESI Fig. 6 and 7,† and main text).

agonists, and lead candidate agents for the lung cancer chemoprevention.

In this study, the acquired binding profiles of top four compounds satisfy some general features, including proper orientation of the protein–substrate interface (AF-2 surface stabilization) and compatibility with the representative of heterodimer PPAR$_\gamma$-RXRα bound to a DNA stretch.[10,15,31] The predicted binding poses of ZINC03775146 (gusperimus) and

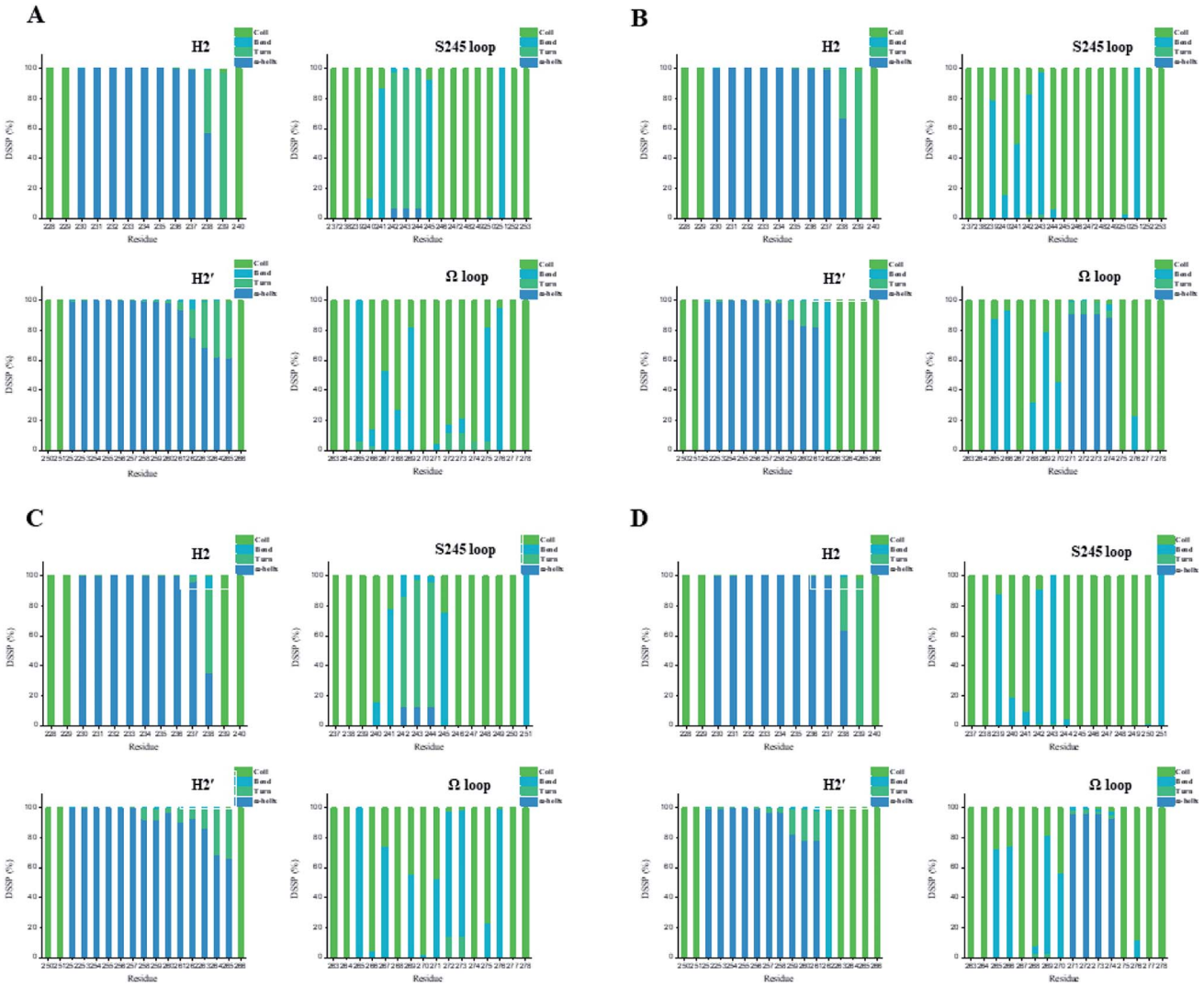

Fig. 7 Secondary structures of H2 & S245 loop (resides 228–240 and residues 237–253) and H2′ & Ω loop (residues 250–266 and residues 263–278) in the (A) ZINC03775146–**Full**, (B) ZINC03831462–**Partial-1**, (C) ZINC14087743–**Full** and (D) ZINC17719775–**Partial-1** complexes. Content rate of turn, α-helix, bend and coil conformations of the individual residues was calculated through the DSSP tool implemented in GROMACS.[49]

ZINC14087743 (miltefosine) also reproduce the adequate structural arrangement for the phosphorylation reaction at the catalytic site (S245 loop), with the necessary flexibility to the β-sheet and Ω loop regions.[11] In addition to the conventional structural adjustments (*e.g.* AF-2), the collaborative structural alterations of H2 & S245 loop and H2′ & Ω loop regions should play an important role in the interaction of Cdk5 with the nuclear receptor, and then affect the phosphorylation of residue Ser245.[68] It means that a structural coupling between H2 & S245 loop and H2′ & Ω loop regions controls $PPAR_{\gamma}$/Cdk5 axis, and $PPAR_{\gamma}$ ligands break the collaborative structural alterations may also hold promise for the drug design, not just on the stabilizations of β-sheets and Ω-loop regions.[11] It is consistent with recent NMR and hydrogen–deuterium exchange (HDX) results that the salt-bridge disruption involving Ω loop and H3 switch are expected to destabilize the AF2 surface.[16] From there, the hydrophobic groups (*e.g.*, biphenyl group) might contribute a lot to the ligand binding with the region and benefit a more effective regulator, on basis of the steric and hydrophobicity/hydrophilicity characteristics of the region between H3, Ω loop and β-sheet of $PPAR_{\gamma}$-LBD (Fig. 1 and 5).[15,57]

4. Conclusion

$PPAR_{\gamma}$ plays a key role in the control of several cellular signaling and gene expression, and is an attractive target for the lung cancer chemoprevention.[3,4] Unfortunately the highly structural dynamic nature of $PPAR_{\gamma}$-LBD adds to not only the difficulties in basic understanding of $PPAR_{\gamma}$ function, but also hinders the rational drug design.[15] To solve the problem, we presented an integrated VS platform (details in Scheme 1) to identify the $PPAR_{\gamma}$ agonists and the binding profiles, with the dynamic behavior of $PPAR_{\gamma}$.

Through the analyses of ligand-binding pocket (LBP) volume and correlated motions of AF-2, β-sheet and Ω loop regions, it

was found that the conformational plasticity of $PPAR_{\gamma}$ is markedly affected by binding of selective agonist (*e.g.* RSG/LRG), and the intrinsically dynamic behavior of $PPAR_{\gamma}$ should be carefully considered in the virtual screening, with multiple acceptable conformations (*e.g.* MD-generated conformations of **Full** and **Partial-1**). The integrated VS platform could quickly sort out favorable compounds (*e.g.* ZINC03775146 (gusperimus) and ZINC14087743 (miltefosine)) and determine their binding profiles, with the considerable balance between accuracies and computational costs. In addition, the intrinsically dynamic behavior of $PPAR_{\gamma}$ aroused a therapeutic window for the regulation of target genes *via* $PPAR_{\gamma}$, using a ligand that blocks kinase accessibility to $PPAR_{\gamma}$ Ser245, and offered hope for resurrecting $PPAR_{\gamma}$-targeted therapeutics to lung cancer chemoprevention.

The recent unified view of drug screening emphasizes that the appropriate selection of the initial structure will determine the success of rational drug design.[69,70] In effect, a considerable proportion of receptors are discovered without the presence of endogenous substrates or synthetic ligands. The allosterically perturbed signals transmit from apo state to ligand bound state (or transition state) can affect the functional activities of receptors. As a result, the presented integrated VS strategy should be of value in the rational drug screening, especially aiming at biomacromolecules with considerable flexibilities or protein–protein association.

Conflicts of interest

The authors have declared that no competing interests exist.

Acknowledgements

The authors wish to thank Professor R. J. Cao for the useful suggestions. This research was supported by the National Natural Science Foundation of China (No. 11774279, 11774280), Fundamental Research Funds for the Central Universities (xzy032020038), China Postdoctoral Science Foundation (2017M613147), Natural Science Basic Research Plan in Shaanxi Province of China (2019JQ-603) and Shaanxi Province Postdoctoral Science Foundation (2017BSHYDZZ44).

References

1 V. G. Keshamouni, R. C. Reddy, D. A. Arenberg, B. Joel, V. J. Thannickal, G. P. Kalemkerian and T. J. Standiford, *Oncogene*, 2004, **23**, 100–108.
2 J. M. Peters, Y. M. Shah and F. J. Gonzalez, *Nat. Rev. Cancer*, 2012, **12**, 181–195.
3 T. H. Chang and E. Szabo, *Cancer Res.*, 2000, **60**, 1129–1138.
4 R. L. Keith and Y. E. Miller, *Nat. Rev. Clin. Oncol.*, 2013, **10**, 334–343.
5 H. Lapillonne, M. Konopleva, T. Tsao, D. Gold, T. McQueen, R. L. Sutherland, T. Madden and M. Andreeff, *Cancer Res.*, 2003, **63**, 5926–5939.
6 Z. C. Dang, V. Audinot, S. E. Papapoulos, J. A. Boutin and C. W. Lowik, *J. Biol. Chem.*, 2003, **278**, 962–967.
7 X. Zuo, Y. Wu, J. S. Morris, J. B. Stimmel, L. M. Leesnitzer, S. M. Fischer, S. M. Lippman and I. Shureiqi, *Oncogene*, 2006, **25**, 1225–1241.
8 S. Prost, F. Relouzat, M. Spentchian, Y. Ouzegdouh, J. Saliba, G. Massonnet, J. P. Beressi, E. Verhoeyen, V. Raggueneau, B. Maneglier, S. Castaigne, C. Chomienne, S. Chretien, P. Rousselot and P. Leboulch, *Nature*, 2015, **525**, 380–383.
9 J. Xia, L. Yang, L. Dong, M. Niu, S. Zhang, Z. Yang, G. Wumaier, Y. Li, X. Wei, Y. Gong, N. Zhu and S. Li, *Front. Pharmacol.*, 2018, **9**, 134.
10 T. S. Hughes, P. K. Giri, I. M. de Vera, D. P. Marciano, D. S. Kuruvilla, Y. Shin, A. L. Blayo, T. M. Kamenecka, T. P. Burris, P. R. Griffin and D. J. Kojetin, *Nat. Commun.*, 2014, **5**, 3571.
11 A. S. Banks, F. E. McAllister, J. P. Camporez, P. J. Zushin, M. J. Jurczak, D. Laznik-Bogoslavski, G. I. Shulman, S. P. Gygi and B. M. Spiegelman, *Nature*, 2015, **517**, 391–395.
12 P. Tontonoz and B. M. Spiegelman, *Annu. Rev. Biochem.*, 2008, **77**, 289–312.
13 A. Farce, N. Renault and P. Chavatte, *Curr. Med. Chem.*, 2009, **16**, 1768–1789.
14 A. J. Kroker and J. B. Bruning, *PPAR Res.*, 2015, **2015**, 816856.
15 I. M. Chrisman, M. D. Nemetchek, I. M. S. de Vera, J. Shang, Z. Heidari, Y. Long, H. Reyes-Caballero, R. Galindo-Murillo, T. E. Cheatham 3rd, A. L. Blayo, Y. Shin, J. Fuhrmann, P. R. Griffin, T. M. Kamenecka, D. J. Kojetin and T. S. Hughes, *Nat. Commun.*, 2018, **9**, 1794.
16 Z. Heidari, I. M. Chrisman, M. D. Nemetchek, S. J. Novick, A. L. Blayo, T. Patton, D. E. Mendes, P. Diaz, T. M. Kamenecka, P. R. Griffin and T. S. Hughes, *Nat. Commun.*, 2019, **10**, 5825.
17 Y. Tanrikulu and G. Schneider, *Nat. Rev. Drug Discovery*, 2008, **7**, 667–677.
18 K. J. Kohlhoff, D. Shukla, M. Lawrenz, G. R. Bowman, D. E. Konerding, D. Belov, R. B. Altman and V. S. Pande, *Nat. Chem.*, 2014, **6**, 15–21.
19 J. Lyu, S. Wang, T. E. Balius, I. Singh, A. Levit, Y. S. Moroz, M. J. O'Meara, T. Che, E. Algaa, K. Tolmachova, A. A. Tolmachev, B. K. Shoichet, B. L. Roth and J. J. Irwin, *Nature*, 2019, **566**, 224–229.
20 Z. Li, S. Chen, C. Gao, Z. Yang, K. C. Shih, Z. Kochovski, G. Yang, L. Gou, M. P. Nieh, M. Jiang, L. Zhang and G. Chen, *J. Am. Chem. Soc.*, 2019, **141**, 19448–19457.
21 Z.-W. Yang, Y.-Z. Zhao, Y.-J. Zang, H. Wang, X. Zhu, L.-J. Meng, X.-H. Yuan, L. Zhang and S.-L. Zhang, *Chin. Phys. Lett.*, 2020, **37**, 058701.
22 Y. Han and P. Kral, *ACS Nano*, 2020, **14**, 5143–5147.
23 R. E. Amaro and W. W. Li, *Curr. Top. Med. Chem.*, 2010, **10**, 3–13.
24 F. Spyrakis and C. N. Cavasotto, *Arch. Biochem. Biophys.*, 2015, **583**, 105–119.
25 W. Evangelista Falcon, S. R. Ellingson, J. C. Smith and J. Baudry, *J. Phys. Chem. B*, 2019, **123**, 5189–5195.
26 R. E. Amaro, J. Baudry, J. Chodera, O. Demir, J. A. McCammon, Y. Miao and J. C. Smith, *Biophys. J.*, 2018, **114**, 2271–2278.
27 C. F. Wong, *J. Theor. Comput. Chem.*, 2019, **18**, 1920001.

28 S. M. Linker, A. Magarkar, J. Kofinger, G. Hummer and D. Seeliger, *J. Chem. Theory Comput.*, 2019, **15**, 4974–4981.
29 Z. Yang, Y. Zhao, D. Hao, S. Ren, X. Yuan, L. Meng and S. Zhang, *J. Biomol. Struct. Dyn.*, 2020, **38**, 1918–1926.
30 J. J. Irwin, T. Sterling, M. M. Mysinger, E. S. Bolstad and R. G. Coleman, *J. Chem. Inf. Model.*, 2012, **52**, 1757–1768.
31 R. T. Nolte, G. B. Wisely, S. Westin, J. E. Cobb, M. H. Lambert, R. Kurokawa, M. G. Rosenfeld, T. M. Willson, C. K. Glass and M. V. Milburn, *Nature*, 1998, **395**, 137–143.
32 R. T. Gampe Jr, V. G. Montana, M. H. Lambert, A. B. Miller, R. K. Bledsoe, M. V. Milburn, S. A. Kliewer, T. M. Willson and H. E. Xu, *Mol. Cell*, 2000, **5**, 545–555.
33 R. Montanari, F. Saccoccia, E. Scotti, M. Crestani, C. Godio, F. Gilardi, F. Loiodice, G. Fracchiolla, A. Laghezza, P. Tortorella, A. Lavecchia, E. Novellino, F. Mazza, M. Aschi and G. Pochetti, *J. Med. Chem.*, 2008, **51**, 7768–7776.
34 P. Larsson, B. Wallner, E. Lindahl and A. Elofsson, *Protein Sci.*, 2008, **17**, 990–1002.
35 Accelrys, *Discovery Studio 3.1*, http://accelrys.com.
36 H. E. Xu, T. B. Stanley, V. G. Montana, M. H. Lambert, B. G. Shearer, J. E. Cobb, D. D. McKee, C. M. Galardi, K. D. Plunket, R. T. Nolte, D. J. Parks, J. T. Moore, S. A. Kliewer, T. M. Willson and J. B. Stimmel, *Nature*, 2002, **415**, 813–817.
37 R. A. Laskowski, J. A. Rullmannn, M. W. MacArthur, R. Kaptein and J. M. Thornton, *J. Biomol. NMR*, 1996, **8**, 477–486.
38 B. R. Brooks, C. L. Brooks 3rd, A. D. Mackerell Jr, L. Nilsson, R. J. Petrella, B. Roux, Y. Won, G. Archontis, C. Bartels, S. Boresch, A. Caflisch, L. Caves, Q. Cui, A. R. Dinner, M. Feig, S. Fischer, J. Gao, M. Hodoscek, W. Im, K. Kuczera, T. Lazaridis, J. Ma, V. Ovchinnikov, E. Paci, R. W. Pastor, C. B. Post, J. Z. Pu, M. Schaefer, B. Tidor, R. M. Venable, H. L. Woodcock, X. Wu, W. Yang, D. M. York and M. Karplus, *J. Comput. Chem.*, 2009, **30**, 1545–1614.
39 M. J. Abraham, T. Murtola, R. Schulz, S. Páll, J. C. Smith, B. Hess and E. Lindahl, *Softwarex*, 2015, **1–2**, 19–25.
40 H. J. C. Berendsen, J. P. M. Postma, W. F. Vangunsteren, A. Dinola and J. R. Haak, *J. Chem. Phys.*, 1984, **81**, 3684–3690.
41 T. Darden, D. York and L. Pedersen, *J. Chem. Phys.*, 1993, **98**, 10089–10092.
42 B. Hess, H. Bekker, H. J. C. Berendsen and J. G. E. M. Fraaije, *J. Comput. Chem.*, 1997, **18**, 1463–1472.
43 X. Daura, K. Gademann, B. Jaun, D. Seebach, W. F. van Gunsteren and A. E. Mark, *Angew. Chem., Int. Ed.*, 1999, **38**, 236–240.
44 C. A. Lipinski, F. Lombardo, B. W. Dominy and P. J. Feeney, *Adv. Drug Delivery Rev.*, 1997, **23**, 3–25.
45 D. F. Veber, S. R. Johnson, H. Y. Cheng, B. R. Smith, K. W. Ward and K. D. Kopple, *J. Med. Chem.*, 2002, **45**, 2615–2623.
46 S. N. Rao, M. S. Head, A. Kulkarni and J. M. LaLonde, *J. Chem. Inf. Model.*, 2007, **47**, 2159–2171.
47 G. Wu, D. H. Robertson, C. L. Brooks 3rd and M. Vieth, *J. Comput. Chem.*, 2003, **24**, 1549–1562.
48 R. Kumari, R. Kumar, C. Open Source Drug Discovery and A. Lynn, *J. Chem. Inf. Model.*, 2014, **54**, 1951–1962.
49 W. Kabsch and C. Sander, *Biopolymers*, 1983, **22**, 2577–2637.
50 P. Schmidtke, V. Le Guilloux, J. Maupetit and P. Tuffery, *Nucleic Acids Res.*, 2010, **38**, W582–W589.
51 B. J. Grant, A. P. Rodrigues, K. M. ElSawy, J. A. McCammon and L. S. Caves, *Bioinformatics*, 2006, **22**, 2695–2696.
52 A. Grossfield and D. M. Zuckerman, *Annu. Rep. Comput. Chem.*, 2009, **5**, 23–48.
53 V. Chandra, P. Huang, Y. Hamuro, S. Raghuram, Y. Wang, T. P. Burris and F. Rastinejad, *Nature*, 2008, **456**, 350–356.
54 S. Lu, Q. Shen and J. Zhang, *Acc. Chem. Res.*, 2019, **52**, 492–500.
55 D. Vidovic, S. A. Busby, P. R. Griffin and S. C. Schurer, *ChemMedChem*, 2011, **6**, 94–103.
56 N. Fresno, M. Macias-Gonzalez, A. Torres-Zaguirre, M. Romero-Cuevas, P. Sanz-Camacho, J. Elguero, F. J. Pavon, F. Rodriguez de Fonseca, P. Goya and R. Perez-Fernandez, *J. Med. Chem.*, 2015, **58**, 6639–6652.
57 A. Laghezza, L. Piemontese, C. Cerchia, R. Montanari, D. Capelli, M. Giudici, M. Crestani, P. Tortorella, F. Peiretti, G. Pochetti, A. Lavecchia and F. Loiodice, *J. Med. Chem.*, 2018, **61**, 8282–8298.
58 N. Brooijmans and I. D. Kuntz, *Annu. Rev. Biophys. Biomol. Struct.*, 2003, **32**, 335–373.
59 H. Wiendl and R. Hohlfeld, *BioDrugs*, 2002, **16**, 183–200.
60 S. Shimakura, M. Kato, K. Saijo, T. Ohno, S. Matsuzaki, N. Tanaka, H. Fukutomi and C. R. Boland, *Gastroenterology*, 1995, **108**, A537.
61 S. Clive and R. C. F. Leonard, *Lancet*, 1997, **349**, 621–622.
62 Y. Zhang, D. Tong, D. Che, B. Pei, X. Xia, G. Yuan and X. Jin, *Int. J. Nanomed.*, 2017, **12**, 605–614.
63 A. Chrdle, Z. Jerhotova, M. Vacik, M. Linka and V. Chmelik, *Int. J. STD AIDS*, 2019, **30**, 94–98.
64 Z. Yang, F. Wu, X. Yuan, L. Zhang and S. Zhang, *J. Mol. Graphics Modell.*, 2016, **65**, 27–34.
65 Z. Yang, Y. Cao, D. Hao, X. Yuan, L. Zhang and S. Zhang, *J. Biomol. Struct. Dyn.*, 2017, 1–14, DOI: 10.1080/07391102.2017.1363661.
66 R. R. Malapaka, S. Khoo, J. Zhang, J. H. Choi, X. E. Zhou, Y. Xu, Y. Gong, J. Li, E. L. Yong, M. J. Chalmers, L. Chang, J. H. Resau, P. R. Griffin, Y. E. Chen and H. E. Xu, *J. Biol. Chem.*, 2012, **287**, 183–195.
67 F. Fratev, *J. Biomol. Struct. Dyn.*, 2017, **35**, 476–485.
68 J. Y. Jang, M. Koh, H. Bae, D. R. An, H. N. Im, H. S. Kim, J. Y. Yoon, H. J. Yoon, B. W. Han, S. B. Park and S. W. Suh, *Biochim. Biophys. Acta, Proteins Proteomics*, 2017, **1865**, 674–681.
69 C. F. Wong and J. A. McCammon, *Annu. Rev. Pharmacol. Toxicol.*, 2003, **43**, 31–45.
70 J. Garcia-Nafria and C. G. Tate, *Annu. Rev. Pharmacol. Toxicol.*, 2020, **60**, 51–71.